The Mode of Incorporation of As(-I) and Se(-I) in Natural Pyrite Revisited

Alain Manceau, Margarita Merkulova, Olivier Mathon, Pieter Glatzel, Magdalena Murdzek, Valentina Batanova, Alexandre Simionovici, Stephan Steinmann, Dogan Paktunc

The mode of incorporation of As(-I) and Se(-I) in natural pyrite revisited

Alain Manceau[*1], *Margarita Merkulova*[*2,§], *Olivier Mathon*[2], *Pieter Glatzel*[2], *Magdalena Murdzek*[2], *Valentina Batanova*[1], *Alexandre Simionovici*[1], *Stephan N. Steinmann*[3], *Dogan Paktunc*[4]

[1]Univ. Grenoble Alpes, CNRS, ISTerre, CS 40700, 38058 Grenoble, France

[2]European Synchrotron Radiation Facility (ESRF), 71 Rue des Martyrs, 38000 Grenoble, France

[3]Univ. Lyon, ENS de Lyon, CNRS, Laboratoire de Chimie, 69342 Lyon, France

[4]Nat. Resources Canada, CanmetMINING, 555 Booth St, Ottawa, ON, Canada

[§]Present address: Department of Geology, University of Liege, B-4000 Liege, Belgium

*Corresponding Authors :

*alain.manceau@univ-grenoble-alpes.fr

*margarit.merkulova@gmail.com

Key words: arsenic, selenium, EXAFS, XANES, Crystal14, ab initio, DFT

ABSTRACT: Pyrite (FeS_2) from coal, sedimentary rocks, and hydrothermal ore deposits generally contains hazardous selenium (Se) and arsenic (As) that are released in natural waters through oxidative dissolution. Knowing the chemical form of As and Se in pyrite has important implication in controlling or preventing their release because the two metalloids accelerate the dissolution of pyrite. Previous extended X-ray absorption fine structure (EXAFS) studies have reported that nominally monovalent As clusters at the sulfur site form As-As pairs at 3.2 Å, whereas monovalent Se does not form Se-Se pairs at this distance for unknown reasons. Here, we revisit this question using As and Se K-edge X-ray absorption near-edge structure (XANES) and EXAFS spectroscopy complemented with atomistic calculations. We find that neither As nor Se atoms can be differentiated from S atom at 3.2-3.3 Å, the cluster and dilute model-fits to As- and Se-EXAFS data yielding equivalent least-squares solutions. Thermodynamic calculations of $Fe_{48}As_3S_{93}$ (3.8 wt.% As) and $Fe_{48}Se_3S_{93}$ (4.0 wt.% Se) structures show that the formation of As-As pairs is energetically favorable and the formation of Se-Se pairs unfavorable. Thus, the equilibrium distribution of As and Se predicted by calculation agrees with published EXAFS data. However, this agreement is incidental because EXAFS fits are ambiguous, the same EXAFS spectra being fit indifferently with a cluster and a dilute model. Regarding Se, the dilute model-fit is probably correct since Se-Se pairs are precluded thermodynamically. The situation is less clear for As. The lowest energy atomic arrangement of As in $Fe_{48}S_{93}As_3$ is similar to the local structure of As in arsenopyrite (FeAsS), thus supporting the cluster model. However, the energy gain to total

energy provided by the formation of As clusters decreases with decreasing As concentration, making them thermodynamically less favorable below 1.0 wt.%. Determining the actual distribution pattern of As in pyrite is challenging.

INTRODUCTION

Arsenic and selenium often substitute for sulfur in pyrite (FeS_2). Arsenic commonly amounts to several thousand mg/kg FeS_2 (ppm) in sedimentary pyrite,[1-7] and can reach up to 10-20 weight-percent (wt.%) in gold deposits.[8-10] The As-Au association has been described in hydrothermal, epithermal, porphyry Cu and Au, Carlin-type and massive volcanogenic gold deposits.[9, 11, 12] In contrast, Se rarely exceeds a few hundred mg/kg for it is 30 to 40 times less abundant then As in the earth crust. Selenious pyrite (Se-pyrite) occurs most frequently in coal[13-16] and shale[17, 18] rocks.

The crystal chemistry of As and Se in pyrite has attracted much interest in the last two decades for economic and environmental reasons. Pyrite often contains Ni, Cu, Sb, and Ag as mineable deposits in addition to Au, and their concentrations are broadly correlated with As.[12, 19-21] However, the mining and smelting of sulfide ores and the processing and combustion of coal release hazardous metal(loid)s, including Hg and Tl besides As and Se.[22-33] It is important to know the modes of incorporation of As and Se in pyrite and their association with trace elements at the atomic scale to recover efficiently and safely valuable metals and to develop better methods of sulfide ore roasting, coal cleaning, and mine waste management.

As and Se have a nominal oxidation state of 1- in FeS_2 and substitute for sulfur in the S_2^{2-} dianion units which coordinate Fe in the pyrite crystal structure (Figure 1a).[34-38] On the basis of their chemical similarity, one would expect As and Se to have similar local structure and atomic distribution. However, As-EXAFS and Se-EXAFS studies on natural pyrite have concluded otherwise.

Savage et al.[36] analyzed an arsenian pyrite (As-pyrite) of average composition $FeAs_{0.02}S_{1.98}$ (1.2 wt.% As) from gold mineralization using As-EXAFS spectroscopy. EXAFS data were fit with one S atom at 2.25 Å in the first coordination shell ($[AsS]_1$), and 4 S atoms at 3.10 Å ($[AsS]_2$) and 3 As atoms at 3.17 Å ($[AsAs]_2$) in the second anionic shell (Figure 1a). The authors concluded that As occurs in clusters in pyrite and explained the lack of detection of $[AsAs]_1$ pairs to the close proximity of 3 $[AsFe]_1$ pairs at 2.32 Å. The lack of $[AsAs]_1$ pairs is consistent with density functional theory (DFT), which predicts that the $AsAs^{2-}$ unit is energetically less favorable than the AsS^{2-} unit.[39] Nanoinclusion of arsenopyrite (FeAsS), which has $[AsS]_1$ and $[AsAs]_2$ pairs in its structure (Figure 1b), was excluded from EXAFS and HRTEM imaging. As clustering in the second S shell around a central As atom was confirmed by Paktunc[35] in arsenian pyrite from Carlin-type gold deposit containing 1.5 mol per cent As ($FeAs_{0.03}S_{1.97}$; 1.6 wt.% As). EXAFS data were fit with 3 $[AsAs]_2$ pairs at 3.24 Å and 2 $[AsS]_2$ pairs at 3.34 Å. The two studies agree with ab initio thermodynamic calculations, which show that pyrite can host up to ~6 wt.% of As ($FeAs_{0.10}S_{1.90}$) in solid solution before unmixing into pyrite-arsenopyrite domains.[40] A compositional segregation of As atoms at a mean concentration of only 1.0 mol per cent As ($FeAs_{0.02}S_{1.98}$) was however unexpected because no $FeAs_2$ mineral isostructural to cubic FeS_2 is known.

Ryser et al.[17] analyzed a Se-pyrite grain containing as much as 0.7 wt.% Se ($FeSe_{0.01}S_{1.99}$) from a mine-waste rock shale using micro XANES and EXAFS spectroscopy. They concluded that Se forms $[SeSe]_1$ pairs at 2.25 Å from the central Se atom and 12 $[SeS]_2$ pairs at 3.24 Å. Matamoros-Veloza et

al. [18], who also studied a shale pyrite by X-ray microspectroscopy but containing ten times less Se (about 600 ppm), fit the EXAFS spectrum from an euhedral grain with a $[SeS]_1$ pair at 2.34 Å and 6 $[SeS]_2$ pairs at 3.20 Å. The two model-fits for Se-pyrite agree in next-nearest neighbor identities, but not in nearest. The Se atoms are dispersed locally in the second study and clustered in the nearest S sites in the first study. Se_2^{2-} dianion units in Se-pyrite are structurally possible because cubic $FeSe_2$, named dzharkenite, occurs naturally in solid solution with pyrite.[41]

EXAFS results obtained on As- and Se-pyrite raise several questions. Why would Se form $[SeSe]_1$ pairs in the nearest S sites and not the next-nearest, and how $[SeSe]_1$ pairs can form at a Se/S atomic ratio of $0.01/1.99 = 5 \times 10^{-3}$? Does it mean that $SeSe^{2-}$ units are more stable than SeS^{2-} units, in contrast to the $AsAs^{2-}$ and AsS^{2-} units? Why is As locally clustered in the next-nearest S sites at an As/S atomic ratio of 0.02/1.98 = 0.01, but not Se at similar Se/As ratio? Here, we address these questions by combining electron microprobe (EPMA) and synchrotron-based X-ray microfluorescence (SXRF) analysis and As and Se K-edge high energy-resolution XANES (HR-XANES) and EXAFS spectroscopy with quantum-mechanical calculations. Five pyrite were studied, two at the As-edge from hydrothermal veins, two at the As- and Se-edge from epithermal and sedimentary deposits, and one at the Se-edge only from another sedimentary deposit.

MATERIALS AND METHODS

The origin and geological setting of the five pyrite are listed in Table 1. Four specimen (Bol, Ger, Sp, Sw) are massive aggregates of pyrite crystals and one (Ut) is a centimeter-sized single crystal (Figure S1). Mineralogical purity was verified by X-ray diffraction (Figure S2). The distributions of As and Se were imaged and their point concentrations measured on polished sections by EPMA using a JEOL JXA-8230 microprobe equipped with five wavelength-dispersive spectrometers (WDS) and an energy-dispersive spectrometer (EDS).[42] As in pyrite Ut and Ger was analyzed also by ICP-AES and Se by ICP-MS to verify the consistency between point and bulk analyses.

Parts of the samples were ground into powder in a glove bag filled with He to prevent oxidation and the powder pressed into pellets for bulk HR-XANES and EXAFS measurements. HR-XANES data were acquired on beamline ID26 at the European Synchrotron Radiation Facility (ESRF, Grenoble) using a multi-crystal analyzer spectrometer.[43] EXAFS data were acquired on beamline BM23 in fluorescence-yield mode using a silicon drift diode detector (SDD). Bulk As-EXAFS was measured on pyrite Bol and Se-EXAFS on pyrite Ut. Growth zones with a wide range of As-Au concentrations were imaged by EPMA in pyrite Bol. A zoned area was relocated by micro SXRF and four As K-edge micro EXAFS spectra were acquired on spots differing in As concentration. The laterally resolved measurements were performed on the microprobe endstation of beamline BM23.[44] The incident beam was focused to 5x5 μm^2 with a set of Pt-coated Kirkpatrick-Baez (K-B) mirrors.

The absolute energy of the HR-XANES spectra is referenced at the As and Se K-edges to the first maximum of the derivative (inflection point) taken to 11870.0 eV for As_2O_3 and to 12658.0 eV for elemental Se (Se^0).[17] The precision of the energy is ± 0.1 eV. The reference compounds arsenopyrite (FeAsS) and realgar (As_4S_4) at the As edge, and ferroselite (orthorhombic $FeSe_2$), achavelite (FeSe), elemental Se, Na_2SeO_3, and Na_2SeO_4 at the Se edge, were diluted to 500 ppm in boron nitride (BN) to prevent overabsorption.[45] Additional methodological information is provided in the Supporting Information (SI).

Atomistic models of As and Se incorporation in pyrite were constructed with DFT using the CRYSTAL14[46] code for periodic systems, and a computational methodology adapted from Smith et al.[47, 48] The hybrid PWGGA functional PW1PW with 20% HF contribution[49] was used for all calculations. The PBEsol0 functional, a hybrid version of the PBEsol XC functional comprising 25% Hartree-Fock (HF) exchange,[50] was used as a check the reliability of the PW1PW functional. The all-electron split-valence 6-311G Pople's basis set[51] was employed for S. An effective core pseudopotential with s411p411d411 external shell was used for Fe[52] in pyrite models doped with As. The TZVP basis set of triple-zeta valence quality with polarization functions was employed for Fe[53] in Se-pyrite models. The As and Se atoms were described with an effective core pseudopotential and the m-pVDZ double-zeta valence with polarization functions basis set.[54]

The PW1PW and PBEsol0 functionals and basis sets were benchmarked by calculating the ionization energies of Fe, S, As and Se (Tables S1-S4), and the precision of the lattice parameters calculated on single unit cells of known structures is assessed (Tables S5-S7). The lattice parameters and interatomic distances derived from our modeling procedure (PW1PW functional) deviate from crystallographic values at most by 1.9% and 2.3% for pyrite,[2] 1.7% and 2.7% for marcasite (orthorhombic FeS_2),[2] 0.8% and 1.9% for arsenopyrite (FeAsS),[55] 1.4% and 2.5% for löllingite (orthorhombic $FeAs_2$),[56] 0.16% and 5.03% for dzharkenite (cubic $FeSe_2$)[57] (Tables S8-S14). The errors are typical for DFT GGA studies.[39, 58-60] The distributions of As and Se were modeled in two supercells of dimensions 2 x 2 x 2 and 3 x 2 x 2. The reciprocal space integration was performed by sampling the Brillouin zone with the 6 x 6 x 6 Pack-Monkhorst mesh,[61] resulting in 112 independent *k* points. Parameter space testing and tolerances for Coulomb and exchange sums are reported in Tables 15 and 16. Additional computational information is provided in SI.

RESULTS

Distribution and concentration of As and Se. Microscopic observations and EPMA mapping show that As and Se are uniformly distributed within the grains of pyrite Ger, Sp, Sw, and Ut (Figure 2). They are free of As- and Se-containing inclusions, such as goldfieldite and colusite sulfide inclusions reported in hydrothermal pyrite.[62] Pyrite Sp contains minute inclusions of chalcopyrite ($CuFeS_2$) observed as brighter scattering spots on backscattered electron (BSE) images. The four pyrite cover a large range of As and Se concentrations (Table 1). As content varies from below the EPMA detection limit of 23 ppm (Sp) to 1590 ppm (Ger), and Se content from below the detection limit of 34 ppm (Sp and Sw) to a maximum of 428 ppm (Ut). Although uniform at the grain scale, As and Se contents vary from grain to grain. As content varies from the detection limit of 23 ppm to 60 ppm in Sw based on the analysis of five grains, and from 50 ppm to 160 ppm in Ut based on the analysis of three grains. Similarly, Se content varies from 318 ppm to 428 ppm in Ut based on three grain analyses.

Growth-zoning compositional variations are observed on the BSE image and EPMA maps of pyrite Bol (Figure S3). On the basis of eight point analyses, As content among the zones varies between 0.15 and 1.14 wt.%, and Se content varies from below the detection limit of 34 ppm to 70 ppm (Table 1). Scatter plots of the fluorescence counts between two elements were derived from each pixel of the EPMA maps, and the co-occurrence between two elements was evaluated from the linear Pearson correlation coefficient ρ. Elemental scatter analysis shows that As and Se are negatively correlated with S (ρ(As-S) = -0.84, ρ(Se-S) = -0.64), and positively correlated together (ρ(As-S) = 0.67) (Figure

S4). Gold (Au) was detected at a concentration of 60 ppm in one spot out of the eight analyzed (detection limit = 47 ppm). The distribution of Au is heterogeneous within pyrite, being localized in growth bands enriched in As (Figure S3). Scatter analysis shows that Au is however weakly correlated to As and Se (ρ(As-Au) = 0.29, ρ(Se-Au) = 0.22) and not to Fe (ρ = -0.01). Elemental correlations have limited chemical significance here, because Au is about three orders of magnitude less concentrated than As and more than four orders less than Fe. Analytical precision is not sufficient to calculate ρ confidently. In addition, the Au and Se fluorescence counts on the EPMA maps represent noise when point concentrations are below the detection limit. These points on the As-Au and Fe-Au correlation plots bias the ρ value. We conclude that the strong negative correlation between abundant As (0.15 – 1.14 wt.%) and major S (ρ(As-S) = -0.84) is evidence for As substitution at the S site. Se probably replaces also S, the lower Pearson correlation (ρ(Se-S) = -0.64) being attributed to the lower Se content, and larger ρ uncertainty thereof.

Formal oxidation state and local structure of As and Se from HR-XANES. Pyrite Bol, Sw, Ut, and Sp were measured at the As K-edge and pyrite Ut, Sp, and Ger at the Se K-edge. The As absorption white line is at 12658.4 eV and the Se white line at 11866.2 eV for all pyrites (Figures 3a and 3b). These edge energies are in the range of those for reduced As and Se compounds and several electronvolts lower than the K edges of oxidized As and Se species (Figures 3c and 3d, Tables S17 and S18). Of the reference spectra, those of arsenopyrite (FeAsS) at the As edge and of arsenopyrite (2 ppm Se) and marcasite (orthorhombic FeS_2, 12 ppm Se) at the Se K-edge provided the best match to the pyrite spectra, confirming the nominal -1 oxidation state of both As and Se in pyrite (Figures 4a-c). Comparison of the pyrite and reference spectra identifies three "indicator" features denoted A, B, and C in Figure 4a.

Region A refers to the energy of the white line. The As edge is at 11865.9 eV for arsenopyrite and 11866.2 eV for pyrite, and the Se edge is at 12657.8 eV for arsenopyrite, 12658.2 eV for marcasite, and 12658.4 eV for pyrite. Region B is situated 32-42 eV above the edge. The pyrite spectra show an absorption hump at this place, which is absent in arsenopyrite and marcasite. The edge energy and structure differences make it possible to distinguish a pyrite host with a corner-linked framework and cubic structure, from arsenopyrite and marcasite with a chain framework and a lower symmetry crystallographic structure (Figure 1). This finding was verified by calculating ab initio the arsenopyrite, marcasite, and pyrite spectra with the finite difference method (FDM) as implemented in FDMNES.[63] The code calculates the final state potential in real space from a cluster of atoms. The form of the potential is not approximated, in contrast to the alternative muffin-tin approach, [64, 65] thus providing a better description of scattering phenomena. The As and Se clusters had a radius of 7 Å and were built from crystallographic structures[2, 55] by replacing S and As with As and Se at the center (As pyrite, Se pyrite, Se marcasite, and Se arsenopyrite). Relaxation of the As and Se sites with CRYSTAL14 did not change the results. Figures 4d-f show that the two XANES fingerprints, edge energy and absorption hump, of As and Se substitution at the S site in pyrite are reproduced theoretically.

Region C is situated 8 eV above the edge energy and corresponds to the first absorption structure after the white line. As-XANES of pyrite has a higher absorption amplitude at 11874.0 eV relative to arsenopyrite. The increase in amplitude is particularly noticeable for Ut (Figure 3a). The energy value of this feature is close to the edge energy of As_2O_5 (11873.6 eV), which suggests that Ut at least, and

perhaps all pyrites, contain some As(V). This species is attributed to the oxidation of arsenic exposed on the surface of pyrite grains.[35]

Local structure of As and Se from EXAFS. Bulk EXAFS spectra measured at the As (pyrite Bol) and Se (pyrite Ut) K-edges are essentially the same, differing only in the amplitude of the oscillations at $k < 4$ Å^{-1} and $k = 10$ Å^{-1} (Figure 5a). They have the same frequency and structure, meaning that As and Se have similar short range order in pyrite. Comparison with the EXAFS spectrum of arsenopyrite (FeAsS) shows that the local coordination of As in this mineral does not replicate that of As and Se in pyrite, in agreement with HR-XANES (Figure 5b). Because Bol is zoned, four micro As-EXAFS spectra were measured at points of interests (POI) selected from the micro As-SXRF map (Figure S5a). There is a factor of three in count rate between the richest (spot 6) and the least (spot 8) As-rich point (Figure S5b). The four spectra have the same frequency and structure and they average out to the bulk spectrum (Figure S6). Thus, zoning reflects varying geochemical conditions during crystallization and does not appear to correlate with the chemical form of As.

Careful study of the As-pyrite spectra from Savage et al. (Clio-2 sample)[36] and Paktunc et al. (grain 218)[35], and the two Se-pyrite spectra from Matamoros-Veloza et al. (POI*a*,*b*)[18] indicates a considerable degree of similarity with our spectra. Since the EXAFS spectra in the previous studies were fit with S atoms in the first shell (i.e., $[AsS]_1$ and $[SeS]_1$ pairs), this infers that As and Se are also bonded to S in our samples. Although this consistency check shows good agreement among different studies in the first anionic shell analysis of As and Se, discrepancies exist in the analysis of the second anionic shell. Savage et al.[36] and Paktunc[35] concluded that As is clustered forming $[AsAs]_2$ pairs, whereas Matamoros-Veloza et al. (POI*a*,*b*)[18] observed $[SeS]_2$ pairs only. How can two EXAFS spectra looking similar, As-pyrite and Se-pyrite, lead to distinct results? We show below that the As- and Se-EXAFS spectra have two least-squares minima in the parameter space.

To obtain robust structural solutions, care was taken to not overparametrize the model-fits. The limit of the number of free parameters in EXAFS fits can be calculated by the Nyquist formula $N = (2\Delta R\Delta k)/\pi$. Nine parameters were adjusted (Table 2), for a number of degrees of freedom in the refinements of $N = [(2 \times (16.0 - 2.7 \text{ Å}^{-1}) \times (3.6 - 1.4 \text{ Å})]/\pi = 18.6$ for As-pyrite and $N = [(2 \times (13.8 - 3.4 \text{ Å}^{-1}) \times (3.6 - 1.4 \text{ Å})]/\pi = 14.6$ for Se-pyrite. Figures 6 and 7 show that the As- and Se-EXAFS spectra can be fit indifferently with a dilute (model 1) and a cluster (model 2) model. In model 1, As and Se are surrounded by 5.9-6.5 S_2 at 3.08-3.09 Å and 5.5-6.1 S_2 at 3.33 Å, and in model 2 by 6.3-6.6 S_2 at 3.15-3.16Å and 4.4-5.7 As_2/Se_2 at 3.16 Å. The metric parameters of the S_1, Fe_1, and Fe_2 shells around As and Se are practically identical in the two models (Table 2). Also included in Figures 6 and 7 are the residual of each fit, which indicates the amount of the spectra unfit by the structural model; the lower the residual, the better the fit. The overlay plots of the fit residuals for each model are identical, therefore the two models equivalent. Consideration of As or Se in the first shell (i.e., As_2^{2-} or Se_2^{2-} dianions) more than doubled the fit residual (model 3 in Figures 6 and 7). The As-S_1 distance is 2.27 Å and the Se-S_1 distance is 2.24 Å, compared to the S-S_1 distance of 2.16 Å in pyrite (Table 2). The differences in bond length match the difference of atomic size between S (1.03 Å), As (1.20 Å), and Se (1.16 Å).

In pyrite, the S_2 shell is split in two sub-shells at 3.08 Å and 3.33 Å. In model 1, the two S_2 distances remain unchanged relative to pyrite while the S_1, Fe_1 and Fe_2 distances are relaxed as a result

of the As and Se for S substitution. In model 2, all interatomic distances are relaxed around the substitutional site. The split of the second anionic shell no longer exists, the S_2 and As_2 atoms being at the same average distance from the central atom (3.15-3.16 Å). The local structure of model 2 is not unrealistic because the As distances to smaller S_2 atoms are not shorter on average than the As distances to bigger As_2 atoms in arsenopyrite (FeAsS).[55] We conclude that the dilute and cluster models are equiprobable from the standpoint of EXAFS analysis. Since EXAFS cannot answer if As and Se are segregated at the local scale, this possibility is examined next by quantum chemical computations.

Equilibrium segregation of As and Se in pyrite. Twelve unique cases of As incorporation schemes and eight unique cases of Se incorporation schemes were tested in total (Figures 8 and S7). Their total and relative energies with respect to the least favorable configuration are given in Table 3, the lattice parameters are reported in Table S19, and Cartesian coordinates are provided in the SI. Formation of As_2^{2-} and Se_2^{2-} dianions (i.e., $[AsAs]_1$ and $[SeSe]_1$ pairs) is energetically unfavorable by more than 6 kcal/mol (models 2Se-2, 3Se-2, 2As-2, 3As-2). The As-As avoidance in the first S shell had been predicted by Blanchard et al.[39] using DFT. Our results show that this theoretical prediction holds for the $[SeSe]_1$ pair. The equilibrium segregation of As and Se in the second S shell was examined by substituting two As/Se atoms for sulfur in a 2 x 2 x 2 supercell ($Fe_{32}(As/Se)_2S_{62}$), and three As/Se atoms for sulfur in a 3 x 2 x 2 supercell ($Fe_{48}(As/Se)_3S_{93}$). The two models have an (As/Se)/S atomic ratio of 0.03, an As concentration of 3.8 wt.%, and a Se concentration of 4.0 wt.%. The FeS_6 octahedra have six short S-S edges of 3.08 Å in length and six long S-S edges of 3.32 Å in length (Figure 1a).[2] The distribution of the As/Se atoms on the long and short edges was varied to examine the energetic preference for clustering on either edge dimension (Figure 8). The main results of this broad evaluation of energy structures are the following:

- As tends to cluster in the second S shell, but not Se regardless of the number and position of the $[SeSe]_2$ pairs on octahedral edges.
- A cluster of 3 As atoms is energetically more favorable than a cluster of 2 As atoms (e.g., models 3As-3 and 3As-5).
- A cluster of 3 As atoms grouped on the same octahedral face, forming an $[As]_3$ triad as in arsenopyrite (Figure 1b), is energetically more favorable than a cluster of 3 As atoms distributed over two octahedral faces (e.g., models 3As-5 and 3As-7).
- Energies of the 3As models show a monotonic trend in function of the dimension of the S-S edge. Larger energy changes (i.e., higher stability) occur for models in which As atoms are distributed on both short and long S-S edges (e.g., models 3As-4, 3As-5, and 3As-6, and models 3As-7 and 3As-8).
- The As-As distances in the second lowest energy structure (model 3As-7) are 3.07 Å, 3.15 Å, and 3.33 Å, close in value to the arsenopyrite $[As]_3$ triad distances of 3.04 Å, 3.19 Å, and 3.34 Å.[55] Model 3As-7 differs by 6 meV/cell from the lowest energy model 3As-8.

Generation of the local order of As in arsenopyrite engenders confidence in the calculations. Also, the fact that the $[As]_3$ arrangement was not found for Se is consistent with the lack of selenious compound structurally analog to arsenopyrite (i.e., FeSeS). Our results also disallow the coexistence of $[SeSe]_1$ and $[SeSe]_2$ pairs, and of $[SeSe]_1$ and $[SeS]_2$ pairs, in pyrite. $[SeSe]_1$ and $[SeSe]_2$ pairs occur in the pyrite isomorph dzharkenite (cubic $FeSe_2$), and therefore can be expected to be energetically

favorable in selenious pyrite. Our results simply suggest that cubic FeS_2 and $FeSe_2$ are not miscible at the atomic scale. This finding may explain why the two compounds do not form a complete solid-solution at the macroscopic scale,[41] the two structures being in this case intergrown at the microscopic scale.

The absence of $[SeSe]_1$ + $[SeS]_2$ pairs in our models conflicts with the results of Ryser and co-workers,[17] who observed their co-existence in a pyrite grain using EXAFS (POI *g* spectrum). On the basis of our results, if Se occurs in the first S shell, then it should also occur in the second S shell to form an $FeSe_2$ local structure. The $FeSe_2$ hypothesis can be dismissed because the POI *g* spectrum differs from that of dzharkenite. Therefore, the alternative consists of hypothesizing that S atoms, not Se, are present in the first shell. This ambivalence was tested by reanalyzing the Se_1 + Fe_1 contribution to EXAFS for POI *g*. Results reproduced in Figure S8 show that the model-fit of Ryser and co-workers[17] is overparametrized, thus the mathematical solution non-unique. When physically meaningful structural constraints are enforced to suppress correlations between parameters, S atoms give a better fit to data than Se atoms. This is in line with Matamoros-Veloza et al.,[18] who fit their pyrite data with a $[SeS]_1$ pair. We conclude that there is a generally good agreement between theoretical predictions and experiments for Se. Se atoms do not cluster in pyrite at the investigated Se/S ratio ≤ 0.03 (4.0 wt.%), and are predicted to demix as cubic $FeSe_2$ if they do at higher molar ratio.

In contrast to Se, the lowest energy structures are those in which As occurs in pairs and triads. Formation of an $[As]_3$ triad in a 3 x 2 x 2 supercell allows an energy gain of 41-47 meV/cell or 5-6 meV per sulfur atom (models 3As-7 and 3As-8). The energy change will be lower, the larger the supercell. Therefore, an $[As]_3$ triad is energetically less likely to form at As/S ≤ 0.03 ([As] ≤ 3.8 wt.%), as in the pyrite samples studied by Paktunc[35] (As/S = 0.015, [As] = 1.6 wt.%), Savage[36] (As/Fe = 0.010; [As] = 1.2 wt.%), and here ($0.001 \leq$ As/S ≤ 0.01; 0.15 wt.% $\leq$ [As] ≤ 1.14 wt.%). To exist at lower As concentration, the As clusters would need to be bigger, as predicted also for the incorporation of Li in MgH_2.[66] In arsenopyrite, each As atom is bonded to three $Fe(S,As)_6$ octahedra, and each octahedron contains an $[As]_3$ triad bonded to the shared As atom (Figure 1b). Transposed to the pyrite structure, a 3 x $[As]_3$ cluster would count 18 As-As pairs in total. Thus, equilibrium segregation of As may exist in pyrite at a weight concentration approaching 1.0 wt.% (As/S = 0.008) as long as the clusters are big enough, but probably not below. In contrast, As clusters likely exist above 2 wt.%, and even more so above 3 wt.%. We conclude that the As cluster models of Paktunc[35] and Savage[36] derived using EXAFS are thermodynamically possible. Arsenic clusters may also form a metastable solid-solution at the nanometer scale precipitated far from thermodynamic equilibrium. Compositional growth zones in pyrite crystals are in fact metastable, and arsenic may very well be inhomogeneously distributed from the micrometer down to the nanometer scale. In conclusion, this study highlights a previously unknown limitation of EXAFS spectroscopy for the study of As and Se in sulfide minerals, which warrants the utmost caution in drawing fine structural distinctions.

ASSOCIATED CONTENT

Supporting Information

The Supporting Information is available free of charge on the ACS Publications website at DOI:

Materials and methods, supplementary tables and figures (PDF)

Cartesian coordinates of the DFT models (XLS)

AUTHOR INFORMATION

Corresponding Authors

E-mail: alain.manceau@univ-grenoble-alpes.fr

E-mail: margarit.merkulova@gmail.com

ORCID

Alain Manceau: 0000-0003-0845-611X

Pieter Glatzel: 0000-0001-6532-8144

Stephan N. Steinmann: 0000-0002-2777-356X

Notes

The authors declare no competing financial interests.

ACKNOWLEDGMENTS

Support was provided by the French National Research Agency (ANR) under grant ANR-10-EQPX-27-01 (EcoX Equipex). The Froggy platform of the CIMENT infrastructure (ANR Grant ANR-10-EQPX- 29-01) and the ESRF provided computing resources. Pierre Girard provided his expertise in parallel scientific processing and Andreas Voegelin from the EAWAG in Zürich provided the arsenopyrite spectrum.

REFERENCES

(1) Smedley, P. L.; Kinniburgh, D. G. A review of the source, behaviour and distribution of arsenic in natural waters. *Appl. Geochem.* **2002,** *17*, 517-568.

(2) Rieder, M.; Crelling, J. C.; Sustai, O.; Drabek, M.; Weiss, Z.; Klementova, M. Arsenic in iron disulfides in a brown coal from the North Bohemian Basin, Czech Republic. *Int. J. Coal Geol.* **2007,** *71*, 115-121.

(3) Jerzykowska, I.; Majzlan, J.; Michalik, M.; Göttlicher, J.; Steininger, R.; Blachowski, A.; Ruebenbauer, K. Mineralogy and speciation of Zn and As in Fe-oxide-clay aggregates in the mining waste at the MVT Zn–Pb deposits near Olkusz, Poland. *Chem. Erde-Geochim.* **2014,** *74*, 393-406.

(4) Stuckey, J. W.; Schaefer, M. V.; Kocar, B. D.; Dittmar, J.; Pacheco, J. L.; Benner, S. G.; Fendorf, S. Peat formation concentrates arsenic within sediment deposits of the Mekong Delta. *Geochim. Cosmochim. Acta.* **2015,** *149*, 190-205.

(5) Biswas, A.; Hendry, M. J.; Essilfie-Dughan, J. Geochemistry of arsenic in low sulfide-high carbonate coal waste rock, Elk Valley, British Columbia, Canada. *Sci. Tot. Environ.* **2016**.

(6) Etschmann, B.; Liu, W. H.; Li, K.; Dai, S. F.; Reith, F.; Falconer, D.; Kerr, G.; Paterson, D.; Howard, D.; Kappen, P., et al. Enrichment of germanium and associated arsenic and tungsten in coal and roll-front uranium deposits. *Chem. Geol.* **2017,** *463*, 29-49.

(7) Wang, Y. H.; Le Pape, P.; Morin, G.; Asta, M. P.; King, G.; Bartova, B.; Suvorova, E.; Frutschi, M.; Ikogou, M.; Pham, V. H. C., et al. Arsenic speciation in Mekong Delta sediments depends on their depositional environment. *Environ. Sci. Technol.* **2018,** *52*, 3431-3439.

(8) Abraitis, P. K.; Pattrick, R. A. D.; Vaughan, D. J. Variations in the compositional, textural and electrical properties of natural pyrite: a review. *Int. J. Miner. Process* **2004,** *74*, 41-59.

(9) Reich, M.; Kesler, S. E.; Utsunomiya, S.; Palenik, C. S.; Chryssoulis, S. L.; Ewing, R. C. Solubility of gold in arsenian pyrite. *Geochim. Cosmochim. Acta* **2005,** *69*, 2781-2796.

(10) Deditius, A. P.; Utsunomiya, S.; Renock, D.; Ewing, R. C.; Ramana, C. V.; Becker, U.; Kesler, S. E. A proposed new type of arsenian pyrite: Composition, nanostructure and geological significance. *Geochim. Cosmochim. Acta* **2008,** *72*, 2919-2933.
(11) Simon, G.; Kesler, S. E.; Chryssoulis, S. Geochemistry and textures of gold-bearing arsenian pyrite, Twin Creeks, Nevada: Implications for deposition of gold in Carlin-type deposits. *Econ. Geol.* **1999,** *94*, 405-421.
(12) Deditius, A. P.; Reich, M.; Kesler, S. E.; Utsunomiya, S.; Chryssoulis, S. L.; Walshe, J.; Ewing, R. C. The coupled geochemistry of Au and As in pyrite from hydrothermal ore deposits. *Geochim. Cosmochim. Acta* **2014,** *140*, 644-670.
(13) Lussier, C.; Veiga, V.; Baldwin, S. The geochemistry of selenium associated with coal waste in the Elk River Valley, Canada. *Environ. Geol.* **2003,** *44*, 905-913.
(14) Diehl, S. F.; Goldhaber, M. B.; Koenig, A. E.; Lowers, H. A.; Ruppert, L. F. Distribution of arsenic, selenium, and other trace elements in high pyrite Appalachian coals: Evidence for multiple episodes of pyrite formation. *Int. J. Coal Geol.* **2012,** *94*, 238-249.
(15) Kolker, A. Minor element distribution in iron disulfides in coal: A geochemical review. *Intern. J. Coal Geol.* **2012,** *94*, 32-43.
(16) Hendry, M.; Biswas, A.; Essilfie-Dughan, J.; Chen, N.; Day, S. Reservoirs of Selenium in Coal Waste Rock, Elk Valley, British Columbia, Canada. *Environ. Sci. Technol.* **2015,** *49*, 8228-8236.
(17) Ryser, A. L.; Strawn, D. G.; Marcus, M. A.; Johnson-Maynard, J. L.; Gunter, M. E.; Moller, G. Micro-spectroscopic investigation of selenium-bearing minerals from the Western US Phosphate Resource Area. *Geochem. Trans.* **2005,** *6*, 1-11.
(18) Matamoros-Veloza, A.; Peacock, C. L.; Benning, L. G. Selenium speciation in framboidal and euhedral pyrites in shales. *Environ. Sci. Technol.* **2014,** *48*, 8972-8979.
(19) Reich, M.; Deditius, A. P.; Chryssoulis, S.; Li, J. W.; Ma, C. Q.; Parada, M. A.; Barra, F.; Mittermayr, F. Pyrite as a record of hydrothermal fluid evolution in a porphyry copper system: A SIMS/EMPA trace element study. *Geochim. Cosmochim. Acta* **2013,** *104*, 42–62.
(20) Large, R. R.; Halpin, J. A.; Danyushevsky, L. V.; Maslennikov, V. V.; Bull, S. W.; Long, J. A.; Gregory, D. D.; Lounejeva, E.; Lyons, T. W.; Sack, P. J., et al. Trace element content of sedimentary pyrite as a new proxy for deep-time ocean-atmosphere evolution. *Earth Planet Sc. Lett.* **2014,** *389*, 209-220.
(21) Gregory, D. D.; Large, R. R.; Halpin, J. A.; Baturina, E. L.; Lyons, T. W.; Wu, S.; Danyushevsky, L.; Sack, P. J.; Chappaz, A.; Maslennikov, V. V., et al. Trace element content of sedimentary pyrite in black shales. *Econ. Geol.* **2015,** *110*, 1389–1410.
(22) Foster, A. L.; Brown, G. E.; Tingle, T. N.; Parks, G. A. Quantitative arsenic speciation in mine tailings using X-ray absorption spectroscopy. *Am. Miner.* **1998,** *83*, 553-568.
(23) Juillot, F.; Ildefonse, P.; Morin, G.; Calas, G.; deKersabiec, A. M.; Benedetti, M. Remobilization of arsenic from buried wastes at an industrial site: mineralogical and geochemical control. *Appl Geochem* **1999,** *14*, 1031-1048.
(24) Diehl, S. F.; Goldhaber, M. B.; Hatch, J. R. Modes of occurrence of mercury and other trace elements in coals from the warrior field, Black Warrior Basin, Northwestern Alabama. *Intern. J. Coal Geol.* **2004,** *59*, 193-208.
(25) Majzlan, J.; Lalinska, B.; Chovan, M.; Jurkovic, L.; Milovska, S.; Göttlicher, J. The formation, structure, and ageing of As-rich hydrous ferric oxide at the abandoned Sb deposit Pezinok (Slovakia). *Geochim. Cosmochim. Acta.* **2007,** *71*, 4206-4220.
(26) Tian, H.; Liu, K.; Zhou, J.; Lu, L.; Hao, J.; Qiu, P.; Gao, J.; Zhu, C.; Wang, K.; Hua, S. Atmospheric emission inventory of hazardous trace elements from China's coal-fired power plants - Temporal trends and spatial variation characteristics. *Environ. Sci. Technol.* **2014,** *48*, 3575-3582.

(27) Ellwood, M. J.; Schneider, L.; Potts, J.; Batley, G. E.; Floyd, J.; Maher, W. A. Volatile selenium fluxes from selenium-contaminated sediments in an Australian coastal lake. *Environ. Chem.* **2016,** *13*, 68–75.

(28) Li, J. W.; Chen, N.; Rajan, I.; Sun, Z.; Wu, H. M.; Chen, D.; Kong, L. The geochemical release feature of Tl in Tl-rich pyrite mine wastes: a long-term leaching test. *Environ. Sci. Pollut. Res.* **2017,** *24*, 12212-12219.

(29) D'Orazio, M.; Biagioni, C.; Dini, A.; Vezzoni, S. Thallium-rich pyrite ores from the Apuan Alps, Tuscany, Italy: constraints for their origin and environmental concerns. *Miner. Deposita* **2017,** *52*, 687-707.

(30) Khamkhash, A.; Srivastava, V.; Ghosh, T.; Akdogan, G.; Ganguli, R.; Aggarwal, S. Mining-related selenium contamination in Alaska, and the state of current knowledge. *Minerals* **2017,** *7*, n° 46.

(31) Lopez-Arce, P.; Garcia-Guinea, J.; Garrido, F. Chemistry and phase evolution during roasting of toxic thallium-bearing pyrite. *Chemosphere* **2017,** *181*, 447-460.

(32) Manceau, A.; Merkulova, M.; Murdzek, M.; Batanova, V.; Baran, R.; Glatzel, P.; Saikia, B. K.; Paktunc, D.; Lefticariu, L. Chemical forms of mercury in pyrite: Implications for predicting mercury releases in acid mine drainage settings. *Environ. Sci. Technol.* **2018,** *52*, 10286-10296.

(33) George, L. L.; Biagionia, C.; Leporeb, G. O.; Lacalamita, M.; Agrosìc, G.; Capitanid, G. C.; Bonaccorsia, E.; d'Acapito, F. The speciation of thallium in (Tl,Sb,As)-rich pyrite. *Ore Geol. Rev.* **2019,** *107*, 364-380.

(34) Simon, G.; Huang, H.; Penner-Hahn, J. E.; Kesler, S. E.; Kao, L. S. Oxidation state of gold and arsenic in gold-bearing arsenian pyrite. *Am. Mineral.* **1999,** *84*, 1071-1079.

(35) Paktunc, D. Speciation of arsenic in pyrite by micro-X-ray absorption fine-structure spectroscopy (XAFS). *Ninth International Congress for Applied Mineralogy* **2008,** *Brisbane, QLD, 8 - 10 September 2008*.

(36) Savage, K. S.; Tingle, T. N.; O'Day, P. A.; Waychunas, G. A.; Bird, D. K. Arsenic speciation in pyrite and secondary weathering phases, Mother Lode Gold District, Tuolumne County, California. *Appl. Geochem.* **2000,** *15*, 1219-1244.

(37) Lowers, H. A.; Breit, G. N.; Foster, A. L.; Whitney, J.; Yount, J. Arsenic incorporation into authigenic pyrite , Bengal Basin sediment , Bangladesh. *Geochim. Cosmochim. Acta.* **2007,** *71*, 2699–2717.

(38) Le Pape, P.; Blanchard, M.; Brest, J.; Boulliard, J. C.; Ikogou, M.; Stetten, L.; Wang, S.; Landrot, G.; Morin, G. Arsenic incorporation in pyrite at ambient temperature at both tetrahedral S^{-I} and octahedral Fe^{-II} sites: Evidence from EXAFS-DFT analysis. *Environ. Sci. Technol.* **2017,** *51*, 150-158.

(39) Blanchard, M.; Alfredsson, M.; Brodholt, J.; Wright, K.; Catlow, C. R. A. Arsenic incorporation into FeS_2 pyrite and its influence on dissolution: A DFT study. *Geochim. Cosmochim. Acta.* **2007,** *71*, 624-630.

(40) Reich, M.; Becker, U. First-principles calculations of the thermodynamic mixing properties of arsenic incorporation into pyrite and marcasite. *Chem Geol* **2006,** *225*, 278-290.

(41) Yakovleva, V. A.; Belogub, E. V.; Novoselov, K. A. Supergene iron sulpho-selenides from the Zapadno-Ozernoe copper-zinc massive sulphide deposit, South Urals, Russia: a new solid-solution series between pyrite FeS_2 and dzharkenite $FeSe_2$. *Min. Mag.* **2003,** *67*, 355-361.

(42) Batanova, V. G.; Sobolev, A. V.; Magnin, V. Trace element analysis by EPMA in geosciences: detection limit, precision and accuracy. *IOP Conf. Ser. Mater. Sci. Eng.* **2018,** *304*, 012001.

(43) Glatzel, P.; Sikora, M.; Smolentsev, G.; Fernandez-Garcia, M. Hard X-ray photon-in photon-out spectroscopy. *Catal. Today* **2009,** *145*, 294-299.

(44) Mathon, O.; Beteva, A.; Borrel, J.; Bugnazet, D.; Gatla, S.; Hino, R.; Kantor, I.; Mairs, T.; Munoz, M.; Pasternak, S., et al. The time-resolved and extreme conditions XAS (Texas) facility at the

European Synchrotron Radiation Facility: The general-purpose EXAFS bending-magnet beamline BM23. *J. Synchrotron Radiat.* **2015,** *22*, 1548–1554.

(45) Manceau, A.; Marcus, M. A.; Tamura, N. Quantitative speciation of heavy metals in soils and sediments by synchrotron X-ray techniques. In *Applications of Synchrotron Radiation in Low-Temperature Geochemistry and Environmental Science*, Fenter, P. A.; Rivers, M. L.; Sturchio, N. C.; Sutton, S. R., Eds. Mineralogical Society of America: Washington, DC, 2002; Vol. 49, pp 341-428.

(46) Dovesi, R.; Orlando, R.; Erba, A.; Zicovich-Wilson, C. M.; Civalleri, B.; Casassa, S.; Maschio, L.; Ferrabone, M.; De La Pierre, M.; D'Arco, P., et al. CRYSTAL14: A Program for the Ab initio investigation of crystalline solids. *Intern. J. Quant. Chem.* **2014,** *114*, 1287-1317.

(47) Smith, F. N.; Taylor, C. D.; Um, W.; Kruger, A. A. Technetium incorporation into goethite (α-FeOOH): An atomic-scale investigation. *Environ. Sci. Technol.* **2015,** *49*, 13699-13707.

(48) Smith, F. N.; Um, W.; Taylor, C. D.; Kim, D. S.; Schweiger, M. J.; Kruger, A. A. Computational investigation of technetium(IV) incorporation into inverse spinels: Magnetite (Fe_3O_4) and trevorite ($NiFe_2O_4$). *Environ. Sci. Technol.* **2016,** *50*, 5216-5224.

(49) Perdew, J. P.; Chevary, J. A.; Vosko, S. H.; Jackson, K. A.; Pederson, M. R.; Singh, D. J.; Fiolhais, C. Atoms, molecules, solids, and surfaces: applications of the generalized gradient approximation for exchange and correlation. *Phys. Rev. B* **1992,** *46*, 6671–6687.

(50) Perdew, J. P.; Ruzsinszky, A.; Csonka, G. I.; Vydrov, O. A.; Scuseria, G. E.; Constantin, L. A.; Zhou, X. L.; Burke, K. Restoring the density-gradient expansion for exchange in solids and surfaces. *Phys. Rev. Lett.* **2008,** *100*, 136406.

(51) Lichanot, A.; Apra, E.; Dovesi, R. Quantum-mechanical Hartree-Fock study of the elastic properties of Li_2S and Na_2S. *Phys. Status Solidi B* **1993,** *177*, 157-163.

(52) Heifets, E.; Kotomin, E. A.; Bagaturyants, A. A.; Maier, J. Thermodynamic stability of stoichiometric $LaFeO_3$ and $BiFeO_3$: a hybrid DFT study. *Phys. Chem. Chem. Phys.* **2017,** *19*, 3738-3755.

(53) Peintinger, M. F.; Oliveira, D. V.; Bredow, T. Consistent gaussian basis sets of triple-zeta valence with polarization quality for solid-state calculations. *J. Comput. Chem.* **2013,** *34*, 451-459.

(54) Heyd, J.; Peralta, J. E.; Scuseria, G. E.; Martin, R. L. Energy band gaps and lattice parameters evaluated with the Heyd-Scuseria-Ernzerhof screened hybrid functional. *J. Chem. Phys.* **2005,** *123*, 174101.

(55) Bindi, L.; Moelo, Y.; Leone, P.; Suchaud, M. Stoichiometric arsenopyrite, FeAsS, from La Roche-Balue quarry, Loire-Atlantique, France: Crystal structure and Mössbauer study. *Can. Miner.* **2012,** *50*, 471-479.

(56) Ondrus, P.; Vavrin, I.; Skala, R.; Veselovsky, F. Low-temperature Ni-rich löllingite from Haje, Pibram, Czech Republic. Rietveld crystal structure refinement. *Neues Jahr. Mineral. Abh.* **2001**, 169-185.

(57) Mandarino, J. A. New minerals recently approved by the commission on new minerals and mineral names, International Mineralogical Association. *Eur. J. Miner.* **1995,** *7*, 447-456.

(58) Peintinger, M. F.; Kratz, M. J.; Bredow, T. Quantum-chemical study of stable, meta-stable and high-pressure alumina polymorphs and aluminum hydroxides. *J. Mater. Chem. A* **2014,** *2*, 13143-13158.

(59) Ghazisaeed, S.; Majzlan, J.; Plasil, J.; Kiefer, B. A simple method for the prediction of the orientation of H_2O molecules in ionic crystals. *J. Appl. Crsyt.* **2018,** *51*, 1116-1124.

(60) Garrett, K. E.; Ritzmann, A. M.; Smith, F. N.; Kessler, S. H.; Devanathan, R.; Henson, N. J.; Abrecht, D. G. First principles investigation of the structural and bonding properties of hydrated actinide (IV) oxalates, $An(C_2O_4)_2.6H_2O$ (An = U, Pu). *Comp. Mater. Sci.* **2018,** *153*, 146-152.

(61) Monkhorst, H. J.; Pack, J. D. Special points for Brillouin-zone integrations. *Phys. Rev. B* **1976,** *13*, 5188–5192.

(62) Merkulova, M.; Murdzek, M.; Mathon, O.; Glatzel, P.; Batanova, V.; Manceau, A. Evidence for syngenetic micro-inclusions of As^{3+}- and As^{5+}-containing Cu sulfides in hydrothermal pyrite. *Am. Miner.* **2019,** *104*, 300-306.
(63) Joly, Y. X-ray absorption near-edge structure calculations beyond the muffin-tin approximation. *Phys. Rev. B* **2001,** *63*, n° 125120.
(64) Ankudinov, A. L.; Rehr, J. J. Relativistic calculations of spin-dependent X-ray-absorption spectra. *Phys. Rev. B* **1997,** *56*, 1712-1716.
(65) Bunau, O.; Joly, Y. Self-consistent aspects of x-ray absorption calculations. *J. Phys. Condens. Matter.* **2009,** *21*, 345501.
(66) Meggiolaro, D.; Gigli, G.; Paolone, A.; Vitucci, F.; Brutti, S. Incorporation of lithium by MgH_2: An ab initio study. *J. Phys. Chem. C* **2013,** *117*, 22467-22477.

FIGURE CAPTIONS

Figure 1. Polyhedral structure and bonding environment of sulfur in pyrite (a) and arsenopyrite (b). Pyrite has a cubic structure consisting of corner-sharing FeS_6 octahedra.[2] Arsenopyrite has a monoclinic structure consisting of single chains of edge-sharing $Fe(As_3S_3)$ octahedra cross-linked by sharing corners.[55] In pyrite, sulfur is bonded to one S atom at 2.16 Å (S_2^{2-} dianion) and to three Fe atoms at 2.26 Å ($[SFe]_1$ pair). The second sulfur shell ($[SS]_2$ pair) is split in two subshells at 3.08 Å (short edges in orange) and 3.32 Å (long edges in green). In arsenopyrite, the As atoms form $[As]_3$ triads on octahedral faces.

Figure 2. Backscattered electron images of pyrite from Bolivia (a), Utah (b), Spain (c), Germany (d), and Switzerland (e), and distributions of As and Se in pyrite Ut, Sp, Ger, and Sw measured by EPMA. The red rectangles indicate the location in the grains of the SXRF maps. Map size: 300 × 80 pixels; pixel size: 2 × 2 μm^2; probe diameter: 2 µm; dwell time 500 ms; electron voltage = 20 kV, current = 500 nA. The pyrite from Bolivia is zoned. The brighter zones in pyrite Sp are chalcopyrite ($CuFeS_2$) inclusions.

Figure 3. As (a) and Se (b) HR-XANES spectra of pyrite. As (c) and Se (d) HR-XANES of reference compounds.

Figure 4. Experimental (a-c) and calculated (d-f) HR-XANES spectra of pyrite measured at the As (a,d) and Se (b,c,e,f) K-edge.

Figure 5. EXAFS spectra of pyrite measured at the As and Se K-edge (a), and pyrite and arsenopyrite measured at the As K-edge (b).

Figure 6. As K-edge EXAFS spectra (a-c) and Fourier transform magnitudes (f-h) of pyrite with model-fits. (d,e) Overlay plots of the fit residuals for models 1 and 2 (d) and models 1 and 3. The peak positions of the Fourier transforms are not corrected for phase shift, and consequently are shifted by $\Delta R \sim$ -0.3 to -0.4 Å relative to structural R distances. *Res* is the fit residual as the goodness-of-fit parameter: $Res = [\Sigma\{|\chi_{exp} - \chi_{fit}|\}/\Sigma\{|\chi_{exp}|\}] \times 100$.

Figure 7. Se K-edge EXAFS spectra (a-c) and Fourier transform magnitudes (f-h) of pyrite with model-fits. (d,e) Overlay plots of the fit residuals for models 1 and 2 (d) and models 1 and 3.

Figure 8. Bonding environment of As in the $Fe_{32}As_2S_{62}$ (a) and $Fe_{48}As_3S_{93}$ (b) equilibrium structures. The S-S edges in yellow are 3.08 Å long and the S-S edges in green are 3.32 Å long in unsubstituted pyrite (Figure 1a). The red line connects the dianionic pair. Distances are in angstrom.

Table 1. List of samples, and As and Se point and bulk concentrations measured by EPMA and ICP-ES/MS

Code name	Origin	Geological setting	[As] EPMA	[As] ICP-ES	[Se] EPMA	[Se] ICP-MS
Bol	Bolivia, MNHN[a] collection, Paris	Hydrothermal vein	0.15-1.14 wt.%	na[b]	bdl – 70 ppm	na
Sw	St Gotthard tunnel, Switzerland	Hydrothermal vein	bdl[c] - 60 ppm (*n*=5)	na	bdl[d]	na
Ut	Park City, Utah, USA	Hydrothermal: epithermal	50-160 ppm (*n*=3)	250 ppm	318-428 ppm (*n*=3)	500 ppm
Sp	Alzo, Gipuzkoa, Spain	Sedimentary	bdl[c] - 30 ppm (n=2)	na	bdl	na
Ger	Neumark, Saxony, Germany	Sedimentary - skarn	na	1590 ppm	na	80 ppm

[a]Museum National d'Histoire Naturelle; [b]Not analyzed; [c]Below detection limit (23 ppm); [d]Below detection limit (34 ppm).

Table 2. EXAFS parameters and interatomic distances in pyrite relative to a central S atom

Pyrite[a]			As Pyrite Bol – Model 1				As Pyrite Bol – Model 2				Se Pyrite Ut – Model 1				Se Pyrite Ut – Model 2			
Atom	*CN*[b]	*R*, Å[c]	Atom	*CN*	*R*, Å	σ[d], Å^2	Atom	*CN*	*R*, Å	σ, Å^2	Atom	*CN*	*R*, Å	σ, Å^2	Atom	*CN*	*R*, Å	σ, Å^2
S	1	2.16	S	1[e]	2.27	0.0031[f]	S	1[e]	2.27	0.0031[f]	S	1[e]	2.24	0.0024[f]	S	1[e]	2.24	0.0024[f]
Fe	3	2.26	Fe	3[e]	2.33	0.0031[f]	Fe	3[e]	2.33	0.0031[f]	Fe	3[e]	2.32	0.0024[f]	Fe	3[e]	2.32	0.0024[f]
S	6	3.08	S	5.9[g]	3.08	0.0056[f]	S	6.3[g]	3.16	0.0058[f]	S	6.5[g]	3.09	0.0040[f]	S	6.6[g]	3.15	0.0038[f]
S	6	3.32	S	6.1[g]	3.33	0.0056[f]	As	5.7[g]	3.16	0.0058[f]	S	5.5[g]	3.33	0.0040[f]	Se	4.4[g]	3.16	0.0038[f]
Fe	3	3.45	Fe	3[e]	3.52	0.0056[f]	Fe	3[e]	3.52	0.0058[f]	Fe	3[e]	3.52	0.0040[f]	Fe	3[e]	3.52	0.0038[f]
			ΔE[h] = 7.0 eV, *Res*[i] = 3.1				ΔE = 7.2 eV, *Res* = 3.4				ΔE = 5.7 eV, *Res* = 3.8				ΔE = 5.3 eV, *Res* = 4.4			

[a]After Rieder et al. [2]; [b]Coordination number; [c]Interatomic distance; [d]Debye-Waller factor; [e]Fixed value; [f]Parameters constrained identical; [g]Sum fixed to twelve; [h]Shift of energy threshold; [i]Fit residual. $Res = [\Sigma\{|\chi_{exp} - \chi_{fit}|\}/\Sigma\{|\chi_{exp}|\}] \times 100$.

Table 3. Calculated total energies of the $FeSe_xS_{2-x}$ and $FeAs_xS_{2-x}$ DFT models, and difference of energy between the dilute and the cluster models

Model	Supercell dimension	Number of Se/As atoms	[Se/As] weight %	Description	Total energy, kcal/mol	difference, kcal/mol	Total energy, eV/cell	difference, eV/cell
2Se-1	222	2	4.0	Two Se atoms at long distance	-41339489.46	0.00	-224081.3463	0.000
2Se-2	222	2	4.0	One [SeSe]1 pair	-41339482.95	-6.52	-224081.3110	-0.035
2Se-3	222	2	4.0	One [SeSe]2 pair on long edge	-41339489.47	0.01	-224081.3464	0.000
2Se-4	222	2	4.0	One [SeSe]2 pair on short edge	-41339489.27	-0.19	-224081.3453	-0.001
3Se-1	322	3	4.0	Three Se atoms at long distance	-62009234.24	0.00	-224081.3465	0.000
3Se-2	322	3	4.0	One [SeSe]1 pair + one [SeSe]2 pair on short edge	-62009227.49	-6.75	-224081.3221	-0.024
3Se-3	322	3	4.0	Three [SeSe]2 pairs on a face with three long edges	-62009234.20	-0.04	-224081.3464	0.000
3Se-4	322	3	4.0	Three [SeSe]2 pairs on a face with two short and one long edge	-62009233.81	-0.43	-224081.3450	-0.002
2As-1	222	2	3.8	Two As atoms at long distance	-18400508.92	0.00	-99740.2451	0.000
2As-2	222	2	3.8	One [AsAs]1 pair	-18400487.67	-21.25	-99740.1299	-0.115
2As-3	222	2	3.8	One [AsAs]2 pair on long edge	-18400513.65	4.73	-99740.2708	0.026
2As-4	222	2	3.8	One [AsAs]2 pair on short edge	-18400513.46	4.54	-99740.2697	0.025
3As-1	322	3	3.8	Three As atoms at long distance	-27600758.17	0.00	-99740.2263	0.000
3As-2	322	3	3.8	One [AsAs]1 pair + one [AsAs]2 pair on short edge	-27600749.32	-8.84	-99740.1943	-0.032
3As-3	322	3	3.8	One isolated As + one [AsAs]2 pair on long edge	-27600763.82	5.65	-99740.2467	0.020
3As-4	322	3	3.8	Two [AsAs]2 pairs on short edges	-27600764.81	6.64	-99740.2503	0.024
3As-5	322	3	3.8	Two [AsAs]2 pairs on long edges	-27600766.07	7.90	-99740.2548	0.029
3As-6	322	3	3.8	Two [AsAs]2 pairs, one on short and another on long edge	-27600767.01	8.84	-99740.2582	0.032
3As-7	322	3	3.8	Three [AsAs]2 pairs on a face with three long edges	-27600769.65	11.48	-99740.2678	0.041
3As-8	322	3	3.8	Three [AsAs]2 pairs on a face with two short and one long edge	-27600771.09	12.92	-99740.2730	0.047

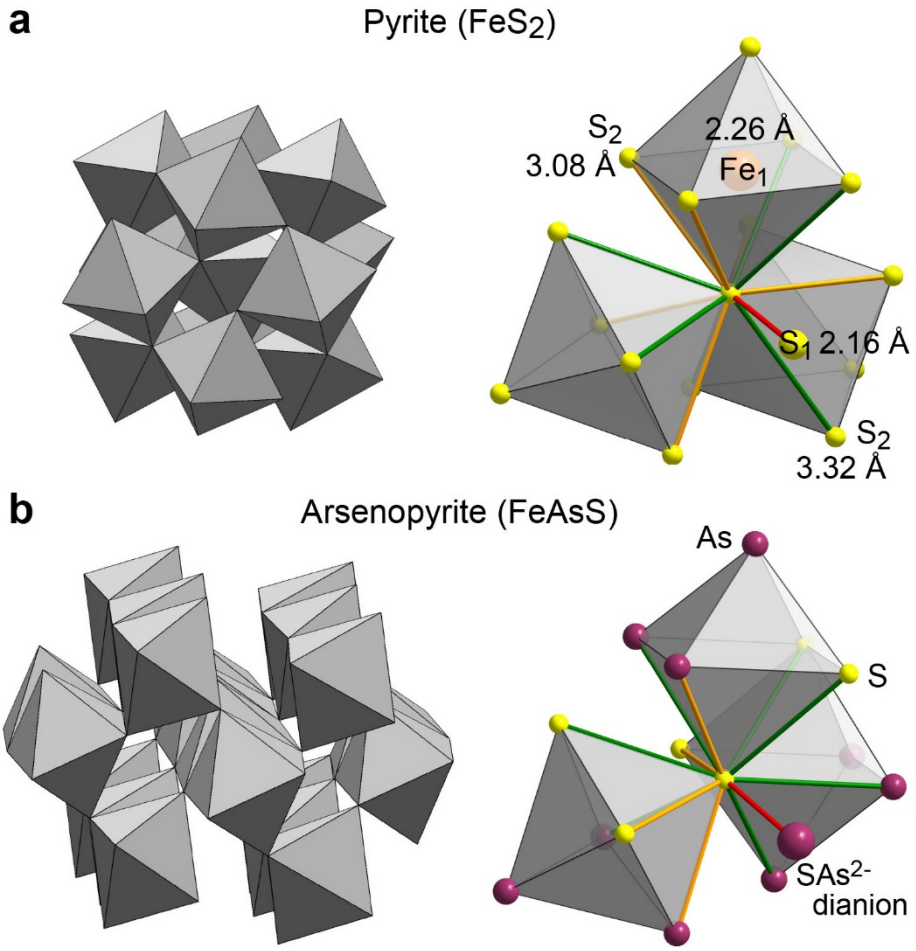
a
Pyrite (FeS_2)
S_2
3.08 Å
2.26 Å
Fe_1
S_1 2.16 Å
S_2
3.32 Å
b
Arsenopyrite (FeAsS)
As
S
SAs^{2-}
dianion

Figure 1

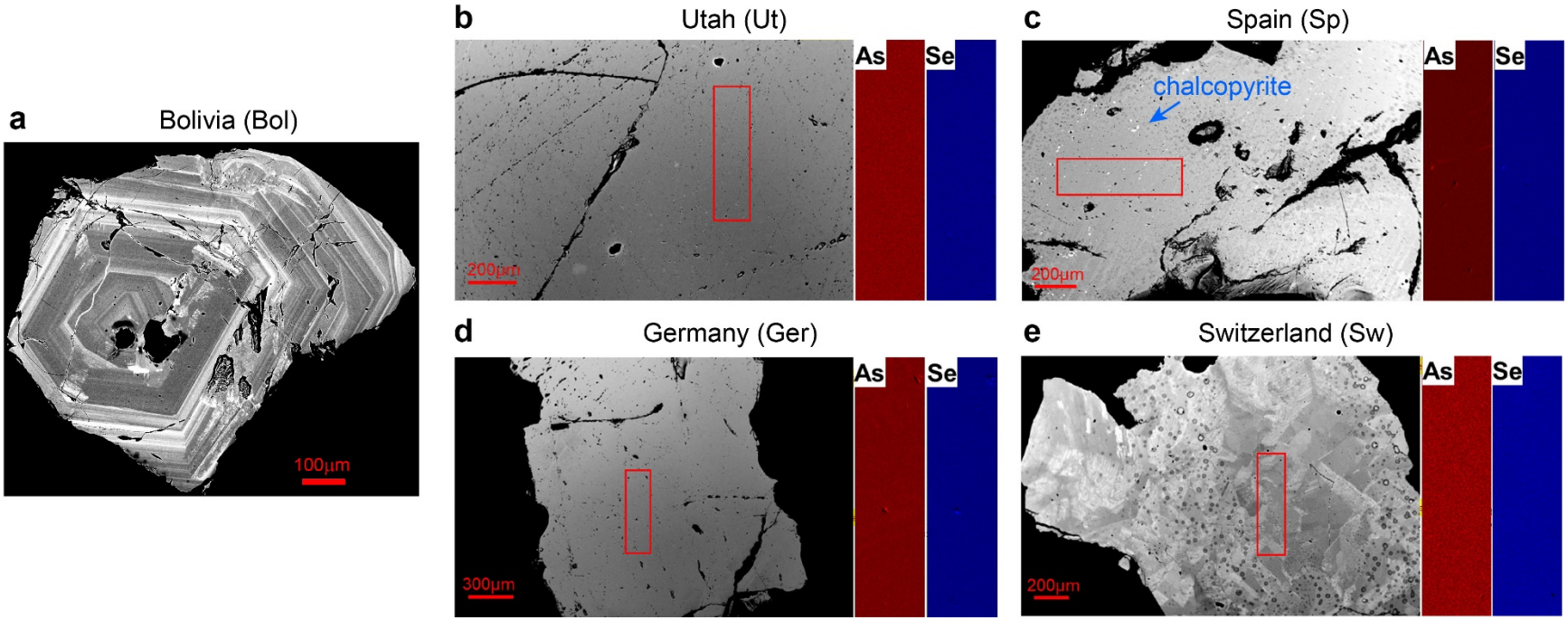

Figure 2

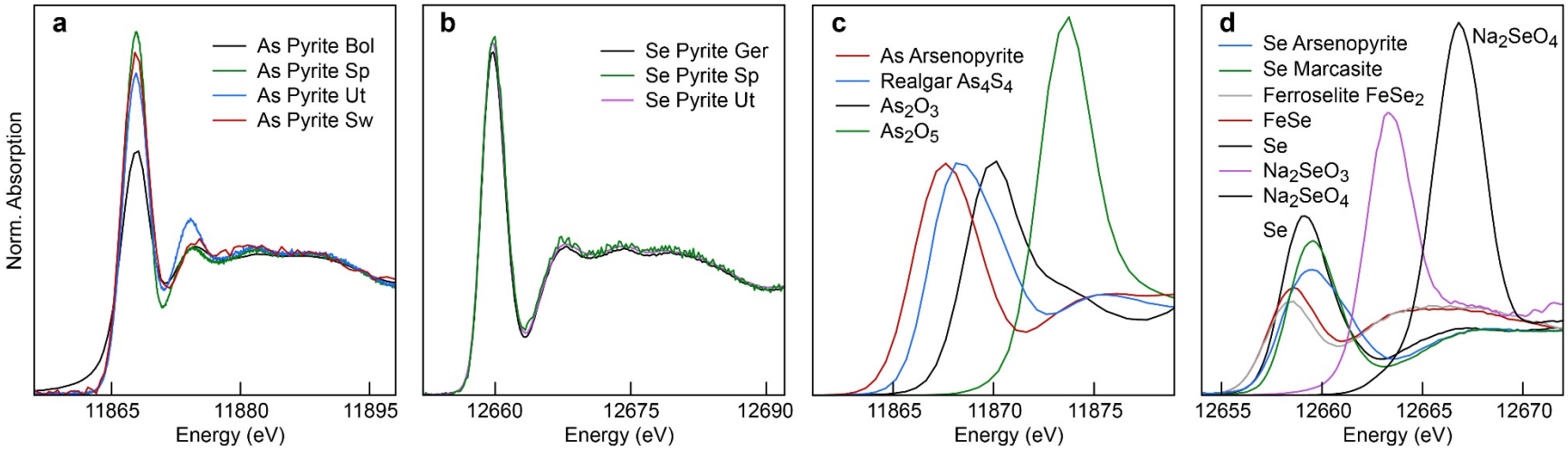

Figure 3

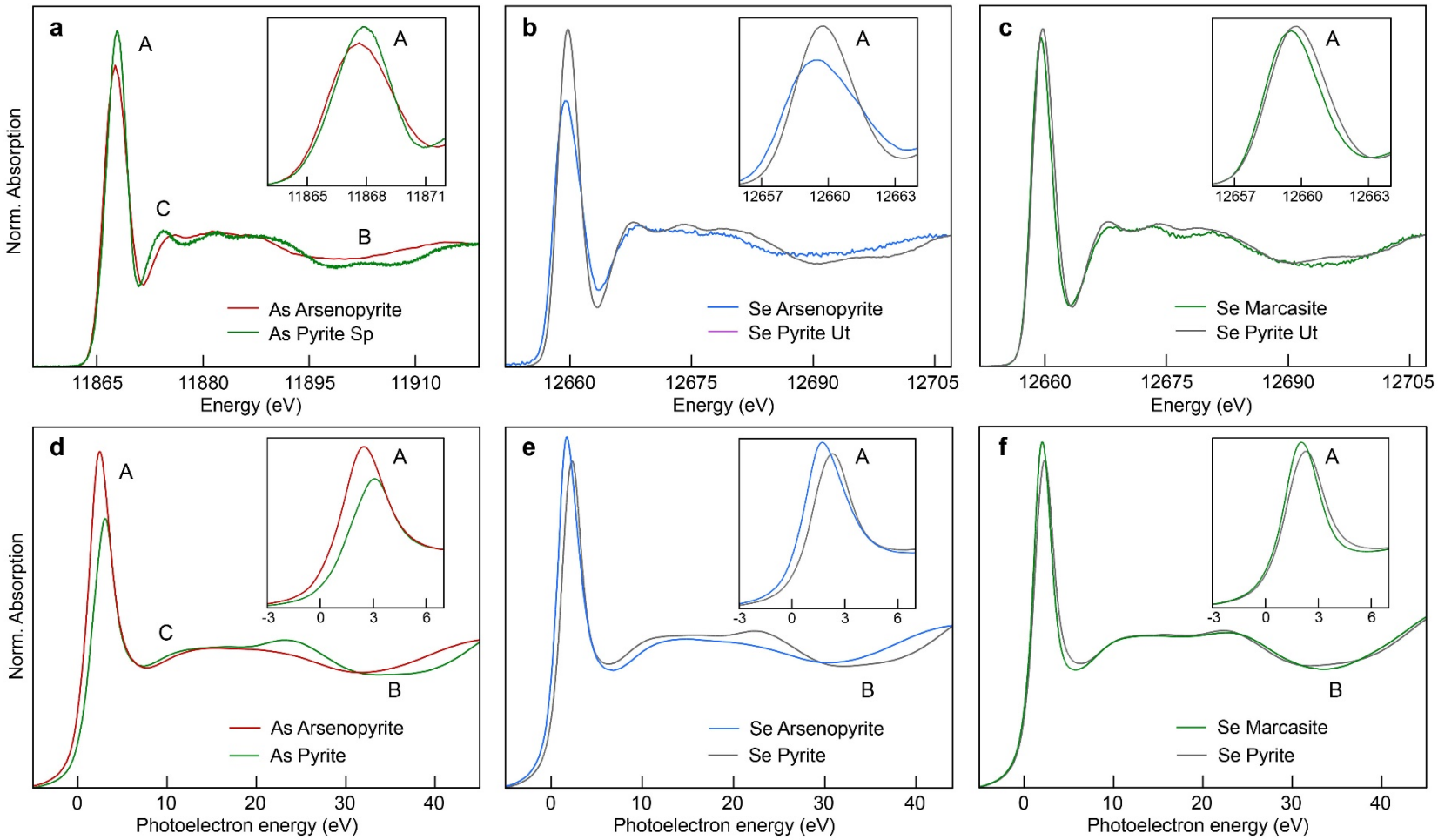
a
A
C
B
As Arsenopyrite
As Pyrite Sp
Norm. Absorption
11865
11880
11895
11910
Energy (eV)
b
Se Arsenopyrite
Se Pyrite Ut
12660
12675
12690
12705
c
Se Marcasite
Se Pyrite Ut
d
As Arsenopyrite
As Pyrite
Photoelectron energy (eV)
e
Se Arsenopyrite
Se Pyrite
f
Se Marcasite
Se Pyrite

Figure 4

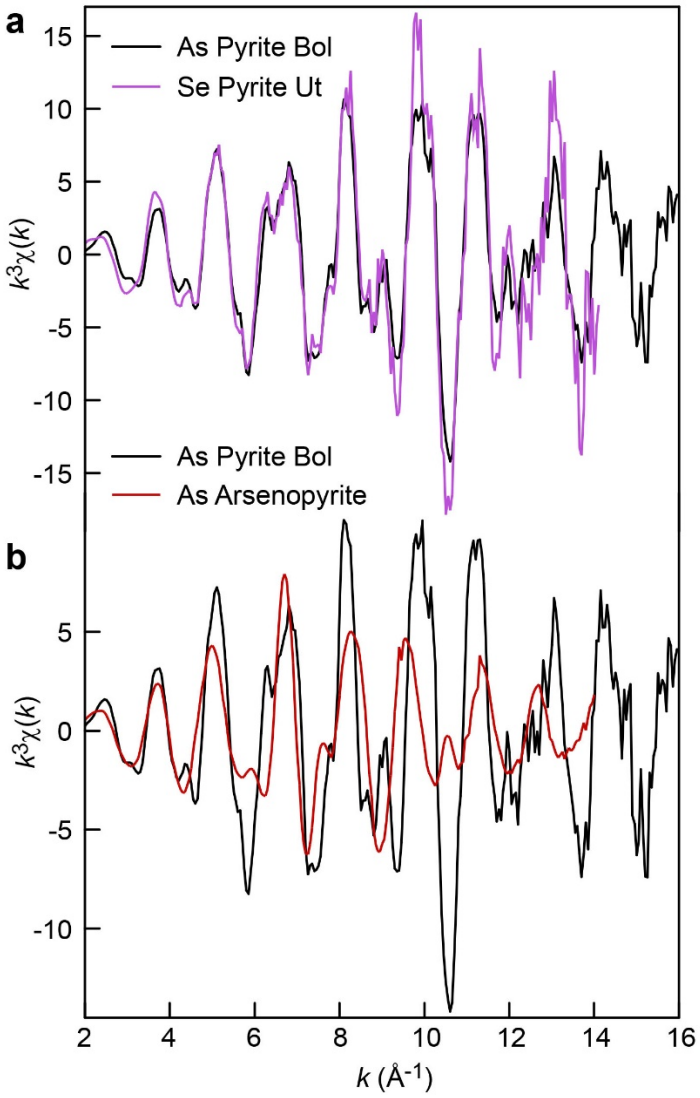
a
As Pyrite Bol
Se Pyrite Ut
$k^3\chi(k)$
15
10
5
0
-5
-10
-15
As Pyrite Bol
As Arsenopyrite
b
5
0
-5
-10
2
4
6
8
10
12
14
16
k (Å^{-1})

Figure 5

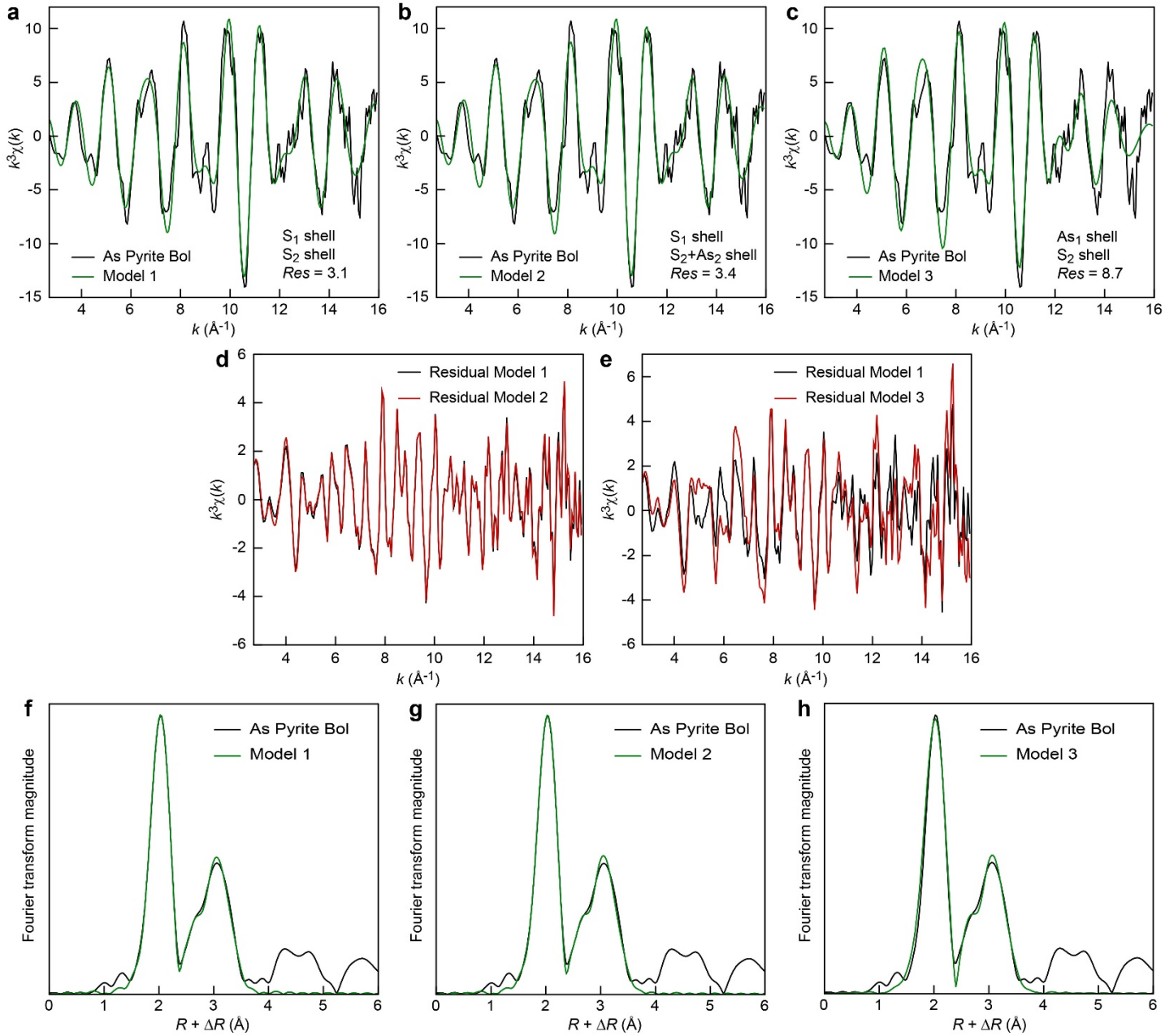
a
b
c
d
e
f
g
h
$k^3\chi(k)$
k (Å^{-1})
As Pyrite Bol
Model 1
Model 2
Model 3
S_1 shell
S_2 shell
Res = 3.1
S_1 shell
S_2+As_2 shell
Res = 3.4
As_1 shell
S_2 shell
Res = 8.7
Residual Model 1
Residual Model 2
Residual Model 3
Fourier transform magnitude
$R + \Delta R$ (Å)

Figure 6

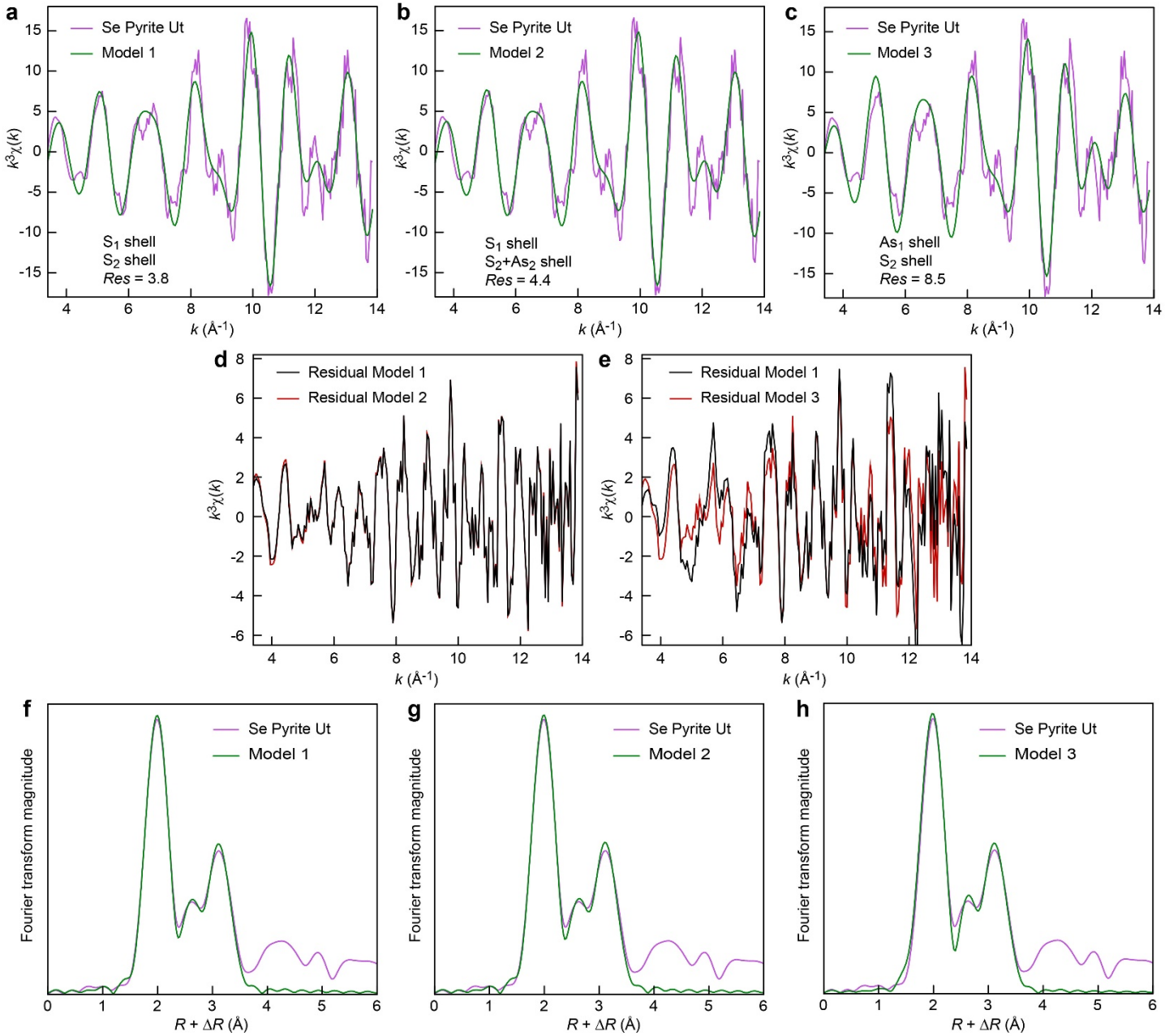
a
Se Pyrite Ut
Model 1
S1 shell
S2 shell
Res = 3.8
b
Se Pyrite Ut
Model 2
S1 shell
S2+As2 shell
Res = 4.4
c
Se Pyrite Ut
Model 3
As1 shell
S2 shell
Res = 8.5
d
Residual Model 1
Residual Model 2
e
Residual Model 1
Residual Model 3
k3χ(k)
k (Å-1)
f
g
h
Fourier transform magnitude
R + ΔR (Å)

Figure 7

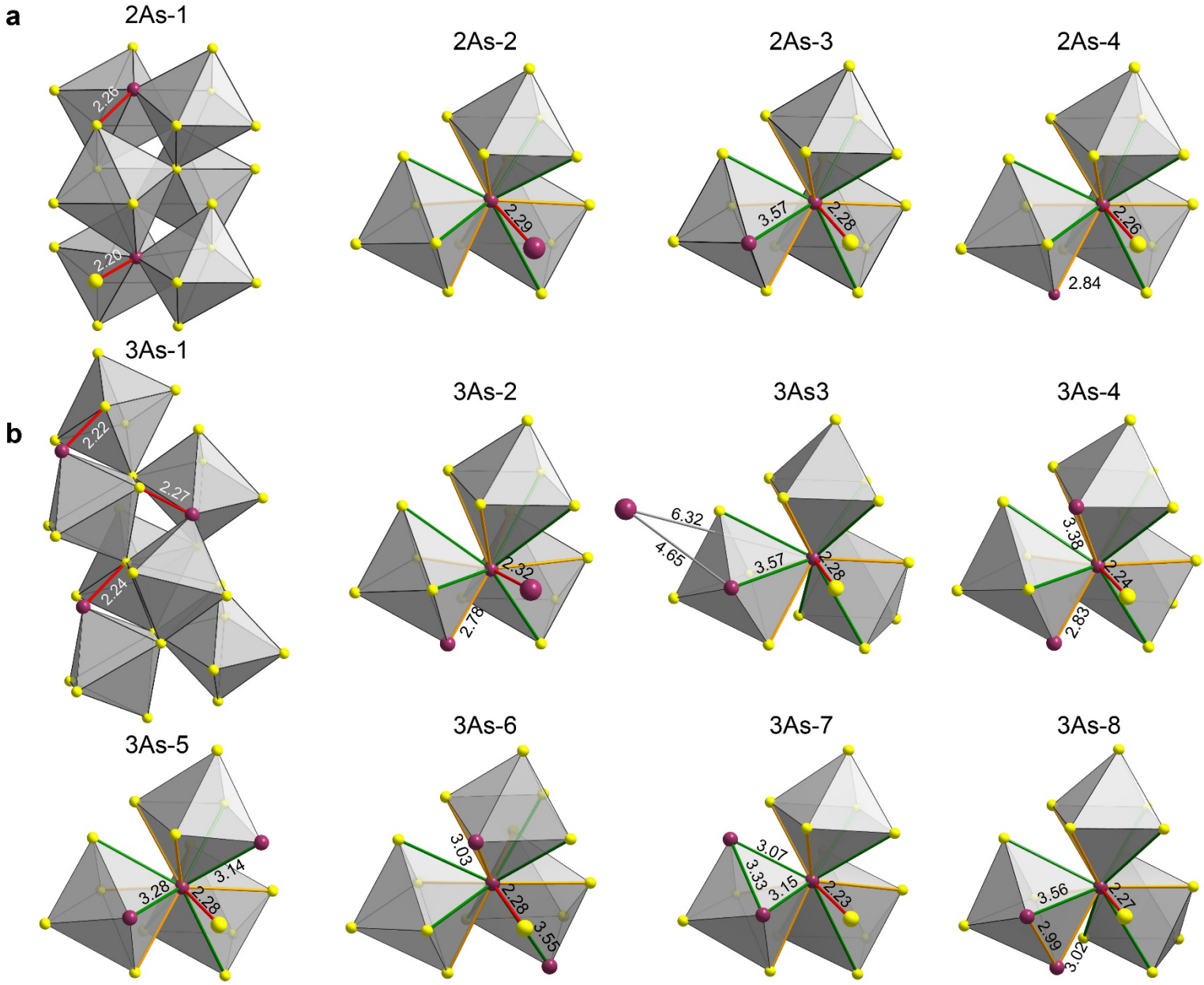
a
2As-1
2.26
2.20
2As-2
2.29
2As-3
3.57
2.28
2As-4
2.26
2.84
b
3As-1
2.22
2.27
2.24
3As-2
2.32
2.78
3As3
6.32
4.65
3.57
2.28
3As-4
3.38
2.24
2.83
3As-5
3.28
2.28
3.14
3As-6
3.03
2.28
3.55
3As-7
3.07
3.33
3.15
2.23
3As-8
3.56
2.99
3.02
2.27

Figure 8